ORIGINAL RESEARCH

Biochar aerogel-based electrocatalyst towards efficient oxygen evolution in acidic media

Bin Hui[1] · Hongjiao Chen[1] · Chengfeng Zhou[1] · Liping Cai[2] · Kewei Zhang[1] · Fengyu Quan[1] · Dongjiang Yang[1]

© The Author(s) 2022

Abstract

The controllable synthesis of oxygen evolution reaction (OER) electrocatalyst is an urgent need to advance the development of sustainable energy conversion and storage. However, the OER efficiency in acidic media is seriously hindered by slow reaction kinetics. The traditional acidic OER electrocatalysts are more prone to be oxidized and corroded as results of unstable carrier structures and variable electronic states of active species. Herein, a high-performing biochar aerogel (BA) based electrocatalyst were realistically designed and synthetized via joint utilization of the terrestrial lignin and seaweed polysaccharide as carbon sources. Originating from the induction effect of "egg-box" structure in alginate and the self-template effect of lignosulfonate, the BA decorated with Ru/RuS_2 particles was synthesized triumphantly. The as-synthesized electrocatalyst required a low overpotential of 228 mV to attain 10 mA cm^{-2} in 0.5 M H_2SO_4 and exhibited a good stability for over 12,000 s. The good activity was strongly dependent on the assembled unique two-dimensional/three-dimensional (2D/3D) channels in carbon aerogels. Notably, the numerous defective sites at carbon could strongly interact with the Ru/RuS_2 heterojunction for remarkably enhancing the catalytic activity and stability of whole catalytic system in acidic media. This work puts forward a novel and effective strategy towards the enhancement of the acidic OER process by rational regulations of the BA and the coupling effect in micro-interface.

Graphical Abstract

🙌 Springer
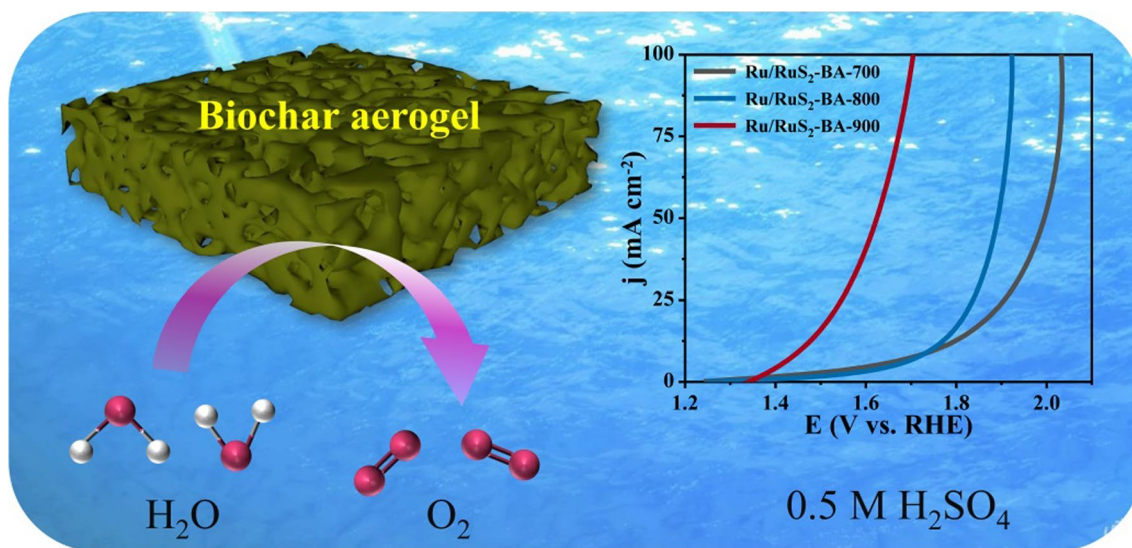
Article Highlights

- A biochar aerogel decorated with Ru/RuS$_2$ particles was synthesized successfully.
- Plenty of defects at carbon were formed due to regulation of two kinds of biomass.
- The sample required a low overpotential of 228 mV at 10 mA cm^{-2} in 0.5 M H$_2$SO$_4$.
- The unique 2D/3D microstructures in biochar aerogel enhanced mass transfer ability.

1 Introduction

The development of clean and sustainable energy has attracted extensive interests due to the shortage and serious environmental pollution of traditional fossil fuels (Hui et al. 2020; Liu et al. 2021a). As a new and clean energy, hydrogen can be generated by water electrosplitting, which is commonly divided into the oxygen evolution reaction (OER) at anode and the hydrogen evolution reaction (HER) at cathode (Chen et al. 2021; Hui et al. 2021). The OER remains as a major challenge because of the rigid O=O bond and the four-electron transfer. Especially, in acid media, the anode material that is comprised of active components and supports is easily oxidized and corroded (Liu et al. 2018; Su et al. 2018; Zhang et al. 2021). Therefore, the improvement of reaction activity and stability of the catalyst system is of vital significance to enhance OER efficiency in acidic conditions. The noble-metal electrocatalysts such as iridium/ruthenium-based materials have been used in acidic OER as their unique electronic structures and relatively excellent stability (Li et al. 2021a; Lin et al. 2019). The ruthenium dioxide has been used as a commercial OER electrocatalyst for large-scale production (Li et al. 2020b; Pascuzzi et al. 2020). Nevertheless, the ruthenium tended to seriously agglomerate in the catalytic process and thus the structure was destroyed in short time (Liu et al. 2021c). The two common strategies for achieving structure stabilization and activity enhancement in acidic OER are as follows: (1) the optimization of electronic structure of Ru via heteroatom doping (such as S, P, or N) (Chen et al. 2020; Li et al. 2020a); (2) the enhancement of interfacial interaction between the active component and carbon carrier (Yang et al. 2021).

As a solid and porous carbon material derived from biomass, the biochar shows potential possibilities to enhance the interfacial contact and regulate the electronic structures of metal species (Jiang et al. 2021; Sakhiya et al. 2020). Compared with carbon-based materials using inorganic raw resources (e.g., carbon nanotubes and graphite) as precursors, the plant biochar exhibits much more porous structures and tunable functionality as well as the low cost, natural abundance and sustainability (Chen et al.

2022; Humagain et al. 2018; Liang et al. 2021). Thanks to the previously mentioned outstanding structural features, biochar is widely used in the field of adsorption, separation, degradation, and energy storage and conversion, etc. (Hua et al. 2022; Lu et al. 2020). As the second biomass resource, lignin is a promising carbon precursor (Liu et al. 2021c; Wang et al. 2018; Wang et al. 2019). Furthermore, the original inert structure of lignosulfonate could be optimized and activated due to the import of S atom (Wang et al. 2021b). However, the pure lignosulfonate solution was very difficult to be converted into a hydrogel and porous carbon aerogel, which impeded its increasing development (Lei et al. 2018). Extracted from marine plants, the alginate with rich carboxyl and hydroxyl groups could strongly chelate with bivalent or trivalent metal ions. The formed unique "egg-box" structures could accelerate the hydrogel formation (Gao et al. 2018; Li et al. 2021b), and then the biochar aerogel (BA) was readily obtained (Kargarzadeh et al. 2018). This type of carbon aerogel showed the high specific surface area and numerous channels. Moreover, the import and removal of heteroatom such as N or S in carbon aerogels made much more lattice defects generated, including edges, disorder, and holes (Yan et al. 2018). These defects in carbon aerogels not only directly acted as the catalytic reaction center, but also possessed strong interaction effect between carbon host and active metals, optimizing electronic structures (Goryaeva et al. 2020), regulating adsorption/desorption energies for reactants (Luo et al. 2021), and enhancing capacities of charge transfer (Musiienko et al. 2021).

In this work, a novel strategy for structural design and synthesis of the BA embedded with Ru/RuS$_2$ heterostructure was proposed for enhancing OER activity and stability in acidic media, using terrestrial lignosulfonate and marine alginate precursors as double carbon sources. Benefiting from the unique induction effect of "egg-box" in alginate and self-template effect of lignosulfonate, the composite hydrogels could be simply formed, and finally converted into polymer aerogels and carbon aerogels via the subsequent freeze-drying and in-situ carbonization. The Ru/RuS$_2$ particles could be well dispersed in the carbon

host. The high temperature treatment not only optimized geometric micro-nanopores and improved graphitization degree, but also greatly contributed to the generation of numerous defective sites in carbon as a result of partial removal of S atoms. Accordingly, the coupling effect between Ru/RuS_2 and carbon host was enhanced significantly. Impressively, the assembled carbon network that comprised of 2D/3D units offered much more micro-channels for the electrolyte transmission. The resulting catalyst required an ultralow overpotential of 228 mV at 10 mA cm^{-2} in 0.5 M H_2SO_4 and exhibited a considerable cycling capacity over 12,000 s. As well as the 2D/3D network microstructure, the strong interaction in micro-interface regions would provide a new method for enhancing activity and stability in acidic medium. This work greatly advances the development for the structural design of BA for enhancing acidic OER process.

2 Materials and methods

2.1 Materials

Ruthenium chloride and sodium lignosulfonate (SL) were purchased from Aladdin Co., Ltd. Sodium alginate (SA), sulfuric acid (98.0 wt.%), and anhydrous ethanol were purchased from Sinopharm Co., Ltd. Nafion solution (5.0 wt.%) was purchased from Sigma-Aldrich Chemical Reagent Co., Ltd. Deionized water was used in the experiment, and all reagents were used directly without further purification.

2.2 Preparation of composite polymer aerogel

Firstly, SL and SA with a mass ratio of 1:1 (Each weight was set as 0.12, 0.24, or 0.36 g) were slowly added to 30 mL deionized water under magnetic stirring after which were completely dissolved, 0.01 or 0.02 g of $RuCl_3$ was added to the above solution. The uniform and transparent hydrogels were obtained. The mixed homogeneous gel solutions were directly freeze-dried for 48 h to form the composite polymer aerogel with multi-channels. The weight ratios of SL/SA and $RuCl_3$ were controlled at 0.12/0.01, 0.24/0.01, 0.36/0.01, 0.12/0.02, 0.24/0.02, and 0.36/0.02, respectively (denoted as 12/1, 24/1, 36/1, 12/2, 24/2, and 36/2, respectively).

2.3 Preparation of Ru/RuS₂-BA electrocatalysts

The aforementioned polymer aerogel was firstly annealed at 350 °C for 3 h (ramping rate: 10 °C min^{-1}). Subsequently, the sample was carbonized at 900 °C for 2 h in Ar atmosphere (ramping rate: 10 °C min^{-1}). The BA decorated with Ru/RuS_2 (denoted as Ru/RuS_2-BA-900) was obtained finally. In order to study the activity of catalysts, the composite polymer aerogel with a mass ratio of 24/1 was also annealed at 700 and 800 °C for 2 h (denoted as Ru/RuS_2-BA-700 and Ru/RuS_2-BA-800, respectively). As a comparison, using only SL or SA as carbon sources and Ru^{3+} ions, the carbon aerogel was also prepared at 900 °C for 2 h (denoted as SL+Ru-900 and SA+Ru-900, respectively).

2.4 Preparation of the Ru/RuS₂-BAs coated on wood carbon (WC)

The poplar wood sample, with a size of 10 mm×10 mm×2 mm, was carbonized at 1000 °C for 2 h, and the WC with multi-channels was obtained. The Ru/RuS_2-BAs prepared with different mass ratios and calcination temperatures were carefully ground into fine powder using agate mortar. 6.0 mg Ru/RuS_2-BA was added to the following solution, consisting of 50 μL Nafion solution, 250 μL anhydrous ethanol, and 250 μL secondary water. The mixed solution was then treated with ultrasound for 30 min, followed by drying at nature air. The formed ink was coated on WC according to the loading weight of 1.0 mg cm^{-2}. The constructed system (Ru/RuS_2-BA@WC) as a self-supported electrode was directly used for the study of electrochemical properties.

2.5 Characterizations

The field emission scanning electron microscopy (FESEM, Quanta 250 FEG, FEI, USA) was used to analyze surface morphologies of the Ru/RuS_2-BAs. The fine nanostructures and elemental distribution of the Ru/RuS_2-BA were characterized by transmission electron microscopy (TEM, JEM-2800F, Japan) with attached energy dispersive X-ray spectroscopy (EDS). The powder X-ray diffraction (XRD, DX2700, China) equipped with Cu $K\alpha$ radiation at a rate (2θ) of 4° min^{-1} ranging from 5° to 90° was used for obtaining phase structures of the Ru/RuS_2-BAs. The chemical states of the catalysts were examined by X-ray photoelectron spectroscopy (XPS) on the ESCALab 250 electron spectrometer from the Thermo Scientific Corporation. Raman spectra were obtained on a laser confocal Raman spectrometer (Thermo Scientific DXR2). The Brunauer–Emmett–Teller (BET, JW-BK132F, Beijing) technique was used to illustrate the specific surface areas. The pore size distribution of catalytic materials was displayed by the adsorption branching spectrum of the isotherm. The precise contents of Ru, S, C, and O elements in Ru/RuS_2-BA were determined by Element analyzer (Elementar Trading, shanghai, UNiCUBE).

2.6 Electrochemical performances evaluation

All OER tests were performed in the 0.5 M H_2SO_4 solution using a CHI 760E electrochemical workstation. In a typical three electrode system, platinum plate was used as a counter electrode, Hg/Hg_2SO_4 was used as a reference electrode, and the working electrode was the self-supported Ru/RuS$_2$-BA@WC. The linear sweep voltammetry (LSV) polarization curves for OER were acquired at a scan rate of 2 mV s^{-1}, and the potentials were corrected by the manual iR compensation. The potentials were converted to the reversible hydrogen electrode (RHE) using the Nernst equation of $E_{RHE} = E_{Hg/Hg2SO4} + 0.645 + 0.0591 \times pH$. The Tafel slope was obtained according to the logarithmic current density of the polarization curve (log[j]) and overpotential (η). The η was calculated using the equation of $\eta = E_{RHE} - 1.23$. The electrochemical impedance spectroscopy (EIS) was achieved with a voltage amplitude of 5 mV in the frequency range of 10 to 100 kHz. The cyclic voltammetry (CV) curves with scan rates of 25, 50, 75, 100, 125, and 150 mV s^{-1} were used to calculate the electrochemical double-layer capacitances (C_{dl}). The cycling stability in the 0.5 M H_2SO_4 solution was obtained using the chronoamperometry method.

3 Results and discussion

### 3.1 Synthesis and morphology of the Ru/RuS$_2$-BA

The schematic illustration for the synthesis of Ru/RuS$_2$-BA is shown in Fig. 1. The lignosulfonate from terrestrial plants and alginate from marine plants, with naturally abundant and sustainable merits, were used as the origin of carbon sources. The Na$^+$ ions from SA were replaced by the partial Ru^{3+} to form a typical "egg-box" structure, while the other part of Ru^{3+} ions were exchanged with Na$^+$ ions from the SL. Due to the strong cross-linking effect of SA, the uniform and well-dispersed composite hydrogel networks that contained both lignosulfonate and alginate macromolecules were easily constructed. After undergoing a freeze-drying process, the composite hydrogel could be successfully converted to a composite polymer aerogel with richly porous structures. The initial pyrolysis at 350 °C was mainly used to stabilize the composite structure and avoid structural collapse in the aerogel. Subsequently, at a much higher temperature, parts of Ru^{3+} ions that were imported were recombined with S source to synthesize RuS$_2$ particles, and the remaining Ru^{3+} ions were changed into Ru particles originating from the carbon reduction. Finally, the Ru/RuS$_2$ heterojunction was confined at carbon aerogels. This kind of synthetic strategy achieved the high-efficiency fixation of sulfur source in biochar-based composites. Notably, at

the high temperature, the S atoms that entered carbocyclic ring in carbon matrix would be partially removed, resulting in the generation of rich defective sites in carbon shells. Recent reports also demonstrated that the high temperature treatment could boost the generation of numerous defective sites at carbon, greatly enhancing the intrinsic OER activity (Zou et al. 2020).

The morphologies of the composite polymer aerogel and the Ru/RuS$_2$-BA are clearly depicted in Fig. 2. As shown in Fig. 2a, the composite polymer aerogel showed a relatively smooth sheet structure, with a thickness of about 1.32 μm. After completing the carbonization at 900 °C, the formed Ru/RuS$_2$-BA-900 exhibited rich pores and complex micro/nanostructures on their surfaces, and the corresponding thickness of the sheet was reduced to 1.18 μm due to the shrinkage effect of the polymer aerogel, as shown in Fig. 2b and Fig. S1, Supporting Information. The thinner sheet and numerous nanopores in Ru/RuS$_2$-BA-900 contributed to the large specific surface area and the fast electrolyte transportation. The elemental mapping images in Fig. S2, Supporting Information, confirmed the homogeneous distribution of the Ru, S, C, and O elements in Ru/RuS$_2$-BA-900. It is revealed in Fig. 2c that Ru/RuS$_2$ had a very small size and was well dispersed at carbon matrix. The carbon with optimized microstructure could enhance the activity and stability of active sites during the OER process in acidic media. The high-angle annular dark-field scanning transmission electron microscopy (HAADF-STEM) image and EDS elemental mappings images in Fig. 2d, e showed that the Ru, S, C, and O elements were distributed evenly. The peaks for C, S, and Ru were easily observed from the EDS spectra in Fig. S3, Supporting Information. Figure 2f shows that the average particle size of Ru/RuS$_2$ was 2.86 nm. The small metal particles could have a strong interaction with carbon host, boosting interfacial charge transfer and thus enhancing the acidic OER process (Guo et al. 2019; Shen et al. 2020).

### 3.2 Fine structures of the Ru/RuS$_2$-BA

Figure 3 displays fine structures of the Ru/RuS$_2$-BA-900. It is revealed in Fig. 3a that the carbon layer in Ru/RuS$_2$-BA-900 had rich nanopores. Both amorphous and graphitized carbon regions were clearly observed in the HRTEM image. The Ru particles with large sizes were gradually decomposed in the initial annealing stage, followed with the generation of small-size Ru particles that were well-dispersed in carbon. The latter highly crystallized Ru boosted the generation of graphitized carbon from amorphous carbon. The graphitized carbon could improve the conductivity and catalytic activity of the whole system. The enlarged dotted box in Fig. 3b clearly shows two lattice distances of 0.205 and 0.323 nm, corresponding to (101) plane for Ru and (111) plane for RuS$_2$, respectively (Liu
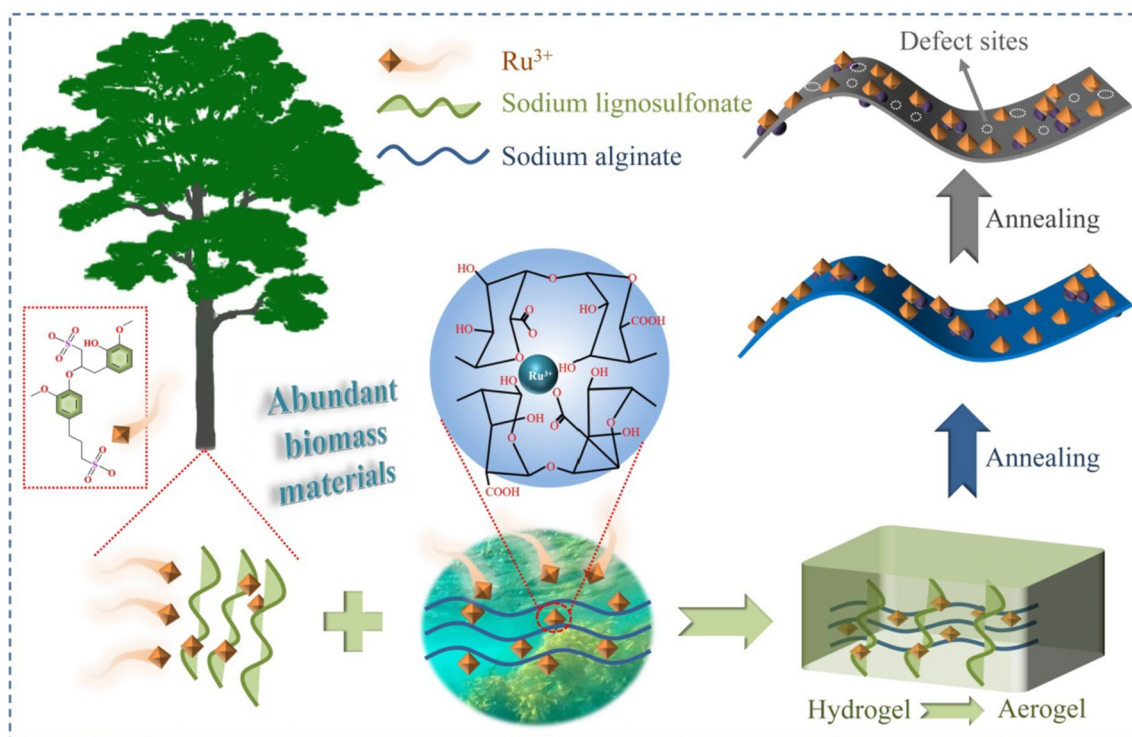
Fig. 1 Schematic illustration of the synthesis process of Ru/RuS$_2$-BA

et al. 2020; Zhu et al. 2021). The marked two continuous Debye rings (Fig. 3c) further demonstrated the coexistence of Ru and RuS$_2$, which was recognized as Ru (101) and RuS$_2$ (111) planes. The X-ray diffraction (XRD) patterns were as well obtained in order to determine microstructure of Ru/RuS$_2$ confined in carbon. As shown in Fig. 3d, the Ru/RuS$_2$-BA-900 displayed typical diffraction patterns of Ru and RuS$_2$. The peaks at 38.24° and 43.98° corresponded to Ru, and the peaks at 27.5°, 31.71°, and 45.36° were in accord with RuS$_2$. However, all those peaks showed a negative shift of about 0.16° compared with the peaks of standard Ru (PDF card # 06-0663) and RuS$_2$ (PDF card # 19-1107). This result might be due to the partial doping of S atoms in aerogel, resulting in the expanded crystal plane spacing of Ru. The carbon aerogels only containing lignosulfonate or alginate were also fabricated in order to testify the regeneration of lignosulfonate/alginate system. The XRD spectra in Figs. S4 and S5, Supporting Information, shows similar graphitic carbon peaks between 20° and 30° while Ru or RuS$_2$ structures in aerogels were not found clearly (Ye et al. 2021). This result was consistent with that of the XRD spectra of the composite polymer aerogel in Fig. S6, Supporting Information. The synergistic effect of lignosulfonate and alginate under the existence of Ru^{3+} ions produced the unique Ru/RuS$_2$ heterostructure. Using the two kinds of promising biomass precursors as carbon sources, the Ru/RuS$_2$ was well confined at BA.

The Raman spectra of carbon aerogels prepared under different conditions were acquired. As shown in Fig. 3e, the characteristic peaks of D band at 1341 cm^{-1} and G band at 1594 cm^{-1} for carbon materials were observed clearly (Zhao et al. 2022). The intensity ratio of I_D/I_G can well show the defect degree of carbon, where the peak of D band reflects lattice defects of carbon atoms, and the peak of G band reflects complete sp^2 hybridization of carbon atoms (Ding et al. 2021; Meng et al. 2021). Specifically, with the increase of carbonization temperature from 700, 800, to 900 °C, the corresponding I_D/I_G values for Ru/RuS$_2$-BAs were 1.07, 1.13, and 1.16, respectively, revealing the production of much larger defect density at a higher temperature (Gabhi et al. 2020; Tian et al. 2020). The high temperature treatment boosted selective separation of some S atoms that had entered carbocyclic ring, and thus inherent carbon defects would be formed at the position of S atoms. Significantly, the Ru/RuS$_2$-BA-900 possessed much more defects compared with biochar of only using lignosulfonate (I_D/I_G 0.92) or alginate (I_D/I_G 1.02) as carbon source at the same temperature of 900 °C. This result affirmed that the import of alginate with inherent "egg-box" microstructure into lignosulfonate is an effective strategy to regulate defect density of carbon materials, as well as the previous-mentioned cross-linked effect to form hydrogel network. The numerous lattice defects such as disorder, edges, and holes in carbon layer could offer more accessible nano-sites and have
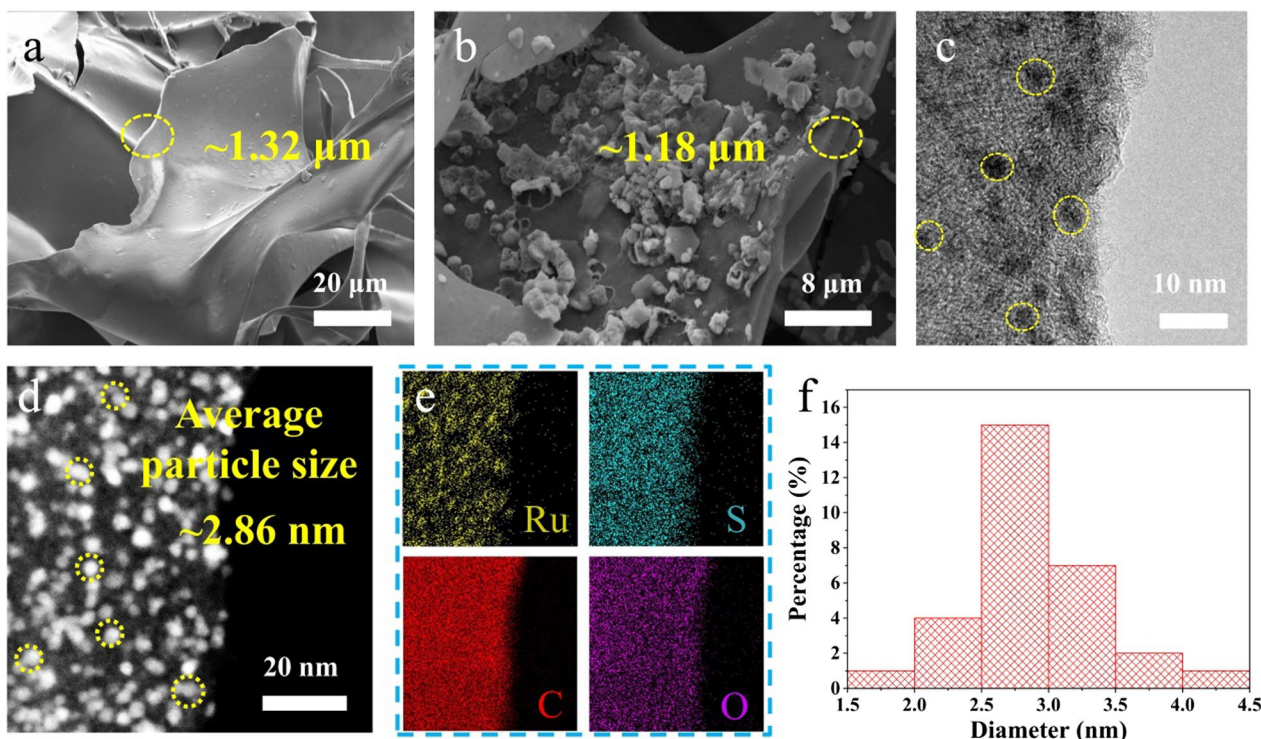
Fig. 2 **a** SEM image of the composite polymer aerogel. **b** SEM, **c** HRTEM, and **d** HAADF-STEM images of Ru/RuS$_2$-BA. **e** EDS mappings images of Ru, S, C, and O elements on Ru/RuS$_2$-BA. **f** Particle size distribution of Ru/RuS$_2$

strong electronic interaction between carbon host and Ru/RuS$_2$ particles, greatly enhancing the acidic OER process.

The nitrogen adsorption isotherms of the Ru/RuS$_2$-BA-900 were obtained from the BET examination, which revealed the specific surface area and pore sizes. As seen in Fig. 4a, the Ru/RuS$_2$-BA-900 showed a specific surface area of 115.54 m^2 g^{-1} which was calculated according to the formula: $P/[V \times (P_0 - P)] = 1/(V_m \times C) + (P/P_0) \times (C - 1)/(V_m \times C)$ (P: Pressure after adsorption equilibrium; P_0: Saturated vapor pressure of adsorbate at adsorption temperature; V: Adsorption quantity of adsorbent to adsorbate at adsorption equilibrium pressure P; V_m: Monolayer saturated adsorption quantity of adsorbent to adsorbate; C: Constants related to the adsorption properties of adsorbents). The larger specific surface area for the Ru/RuS$_2$-BA-900 was conducive to the fast transportation of electrolyte and adequate exposure of numerous active sites. The curve showed the typical hysteresis phenomenon, corresponding to type IV isotherms. This result indicated that there were abundant nanopores in carbon-based materials (Liu et al. 2021b). In Fig. 4b, it is observed that the average size of pores was about 3.94 nm, implying that the carbon material owned much more mesopores and a small part of micropores. The *in-situ* carbonization for the composite polymer aerogel brought about plenty of

nanopores because of the shrinking effect of the polymer aerogel itself and the escape of partial S species. The XPS spectrum of the Ru/RuS$_2$-BA-900 is depicted in Fig. 4c, where the peaks for S$_{2p}$, C$_{1s}$ + Ru$_{3d}$, and O$_{1s}$ are found clearly. The element analyzer results in Fig. S7, Supporting Information, show that the mass fractions of Ru, S, C, and O were 2.21 wt.%, 7.25 wt.%, 56.45 wt.%, and 34.09 wt.%, respectively. The S$_{2p}$ spectra in Fig. 4d show three peaks at 163.0, 164.2, and 169.8 eV, which corresponded to the S$_{2p3/2}$, S$_{2p1/2}$, and S–O bonds, respectively (Xu et al. 2021; Zhu et al. 2021). As found in Fig. 4e, the spectra of C$_{1s}$ and Ru$_{3d}$ overlap. The two peaks located at 280.8 and 285.7 eV corresponded to Ru^0 and Ru^{4+}, respectively, and the other two peaks at 284.8 and 289.0 eV were attributed to the standard peak of carbon and C=O, respectively (Xia et al. 2020). This result further indicated the successful formation of Ru/RuS$_2$ heterostructure. The S atoms with negative charge were conducive to be captured by that of positive charge, leading to the generation of RuS$_2$. The Ru/RuS$_2$ heterostructure was expected to have faster charge transfer capacity compared with that of only Ru or RuS$_2$ particles during the OER process. The O$_{1s}$ spectra in Fig. 4f display three peaks at 532.8, 533.8, and 535.8 eV, which agreed with C=O bond, O–C bond, and adsorbed water molecules on the surface (Fan et al. 2019).
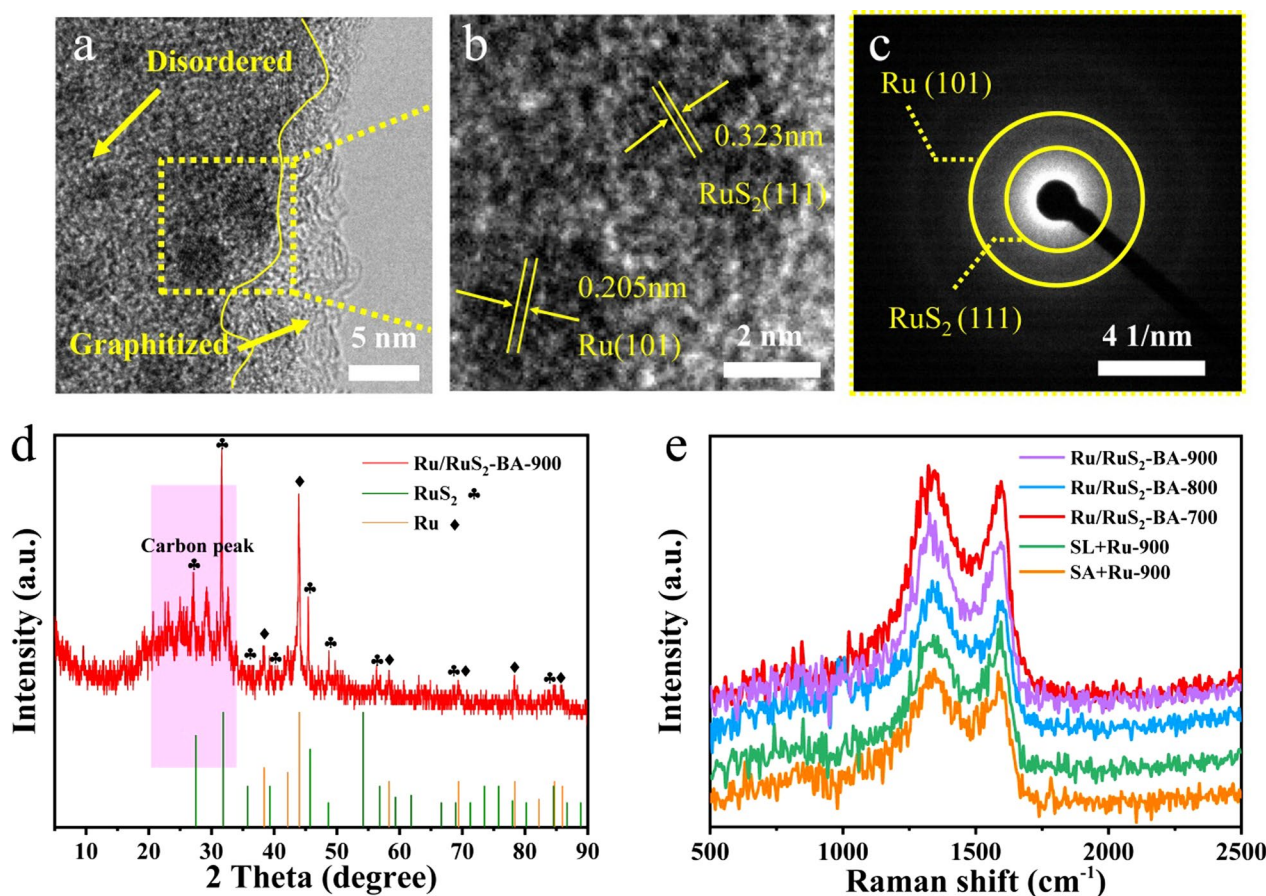
Fig. 3 **a**, **b** HRTEM images of Ru/RuS₂-BA-900. **c** Selected area electron diffraction (SAED) of Ru/RuS₂-BA-900. **d** XRD patterns of Ru/RuS₂-BA-900, **e** Raman spectra of SL + Ru-900, SA + Ru-900, and Ru/RuS₂-BAs prepared at 700, 800, and 900 °C

3.3 OER performances of the Ru/RuS₂-BA

The ink that was composed of Ru/RuS₂-BAs and Nafion was coated onto a porous and conductive WC. The assembled electrode was directly used for the evaluation of electrocatalytic OER in acidic media. Fig. S8 in Supporting Information, shows the resistance value of about 7.0 Ω for WC. Compared with that of the pristine wood (Fig. S9 in Supporting Information), the wall layer for WC in Fig. S10, Supporting Information, became thinner, implying an increase in specific surface area. High temperature treatment could significantly improve conductivity of wood. In addition, the WC was mainly composed of carbon element, which would be more stable in acid electrolyte. The WC with high stability offered high-efficiency proton transport during the OER process. Hence, the WC as the self-supported substrate not only inherited the porous structure of the pristine wood but also its conductivity and stability were enhanced remarkably. In order to explicitly compare the activity of the electrocatalyst, the performance of WC was tested. The result showed that the WC had almost no OER performance (Fig. S12 in

Supporting Information). Accordingly, the self-supported nanoelectrode of Ru/RuS₂-BAs on WC (denoted as Ru/RuS₂-BAs@WC) was designed. The OER activity in 0.5 M H_2SO_4 for the Ru/RuS₂-BAs@WC is shown in Fig. 5. In order to explore activities of various Ru/RuS₂-BAs, the mass ratios of the SL-SA and $RuCl_3$ were changed to 12/1, 24/1, 36/1, 12/2, 24/2, and 36/2, respectively (the temperature was set as the same temperature of 900 °C). In Fig. 5a, the OER activity of the Ru/RuS₂-BA-900@WC prepared with the mass ratio of 24/1 is superior to that of aforementioned other conditions. According to the linear sweep voltammetry (LSV), when the content of $RuCl_3$ was 0.01 g, the Ru/RuS₂-BA-900@WC prepared with mass rations of 12/1, 24/1, and 36/1 required overpotentials of 447, 228, and 223 mV at a current density of 10 mA cm⁻², respectively. However, the Ru/RuS₂-BA-900@WC prepared with the mass ratio of 24/1 showed better catalytic activity, requiring overpotential of 474 mV to reach 100 mA cm⁻², which was lower than the sample prepared with the mass ratio of 36/1. In order to further investigate the activity of the catalyst, the $RuCl_3$ content was increased to 0.02 g and the mass ratios of the
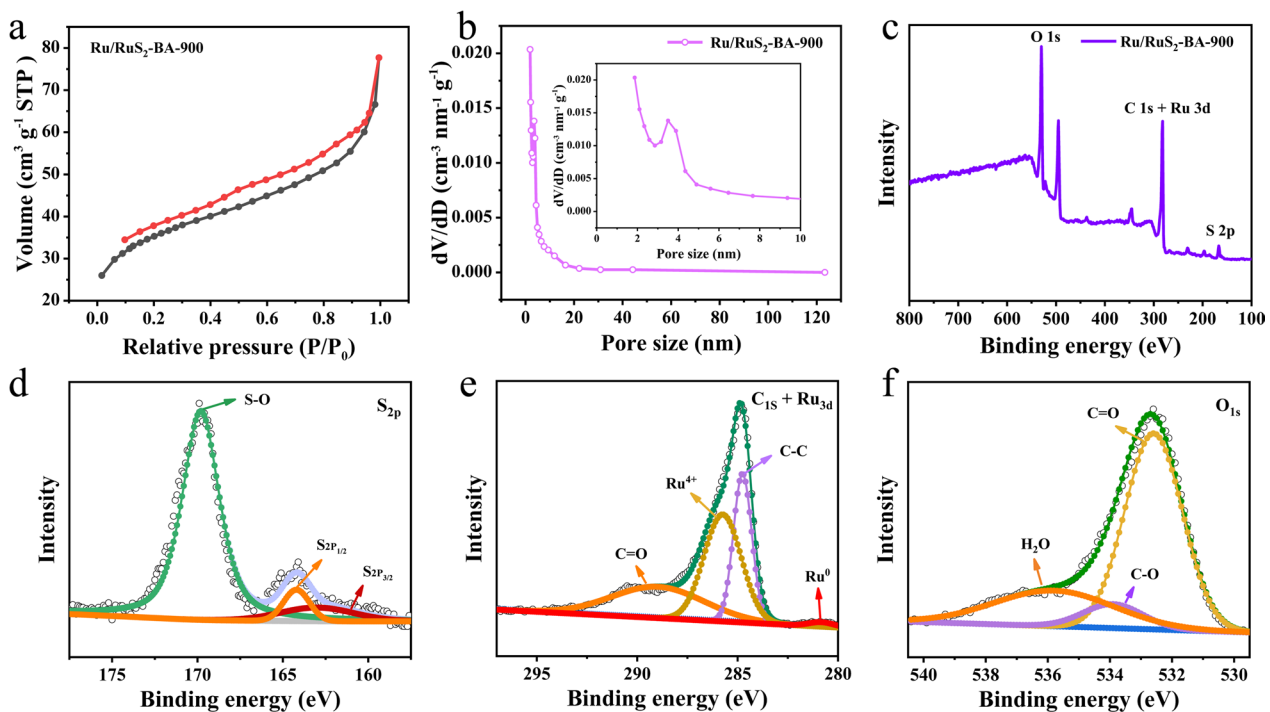
Fig. 4 **a** Nitrogen adsorption isotherms and **b** Pore size distribution of Ru/RuS$_2$-BA-900. **c** XPS survey spectrum of the Ru/RuS$_2$-BA and corresponding high-resolution XPS spectra for **d** S$_{2p}$, **e** C$_{1s}$+Ru$_{3d}$, and **f** O$_{1s}$

SL-SA were the same as the aforementioned changes. It was observed that the sample prepared with the mass ratio of 12/2 exhibited better catalytic activity than that prepared with the mass ratio of 12/1. However, the catalytic activity for samples prepared with the mass ratio of 24/2 and 36/2 was poorer than that of 24/1 and 36/1, respectively. The appropriate ratio of Ru in the catalyst could enhance catalytic performance of whole system, but a large amount of Ru particles were more prone to aggregate, which would inhibit the formation of Ru/RuS$_2$. In addition, the aggregation of Ru would also lead to the dissolution of partial catalyst in acidic media, causing decline of the catalytic activity and stability. Figure 5b shows the corresponding semicircle-like electrochemical impedance spectroscopy (EIS) curve, revealing the charge transfer capability of Ru/RuS$_2$-BAs@WC. The Ru/RuS$_2$-BA-900@WC prepared with a mass ratio of 24/1 showed the lowest R_{ct} value, confirming excellent charge transport ability and accelerated reaction kinetics. The charge transfer resistance of Ru/RuS$_2$-BAs@WC was increased with the increase of the Ru content. The larger charge transfer resistance for the electrocatalyst with more Ru could be ascribed to the serious aggregation in particles. Figure 5c shows the Tafel plots of the Ru/RuS$_2$-BAs@WC prepared with different mass ratios. The Tafel slope for the sample prepared with the mass ratio of 24/1 was the smallest (40.0 mV dec^{-1}), representing fastest reaction kinetics during OER. The Ru/RuS$_2$-BA-900@WC prepared with 0.02 g

Ru exhibited an increasing Tafel slope, meaning a relatively sluggish reaction. The effects of the carbonization temperature on the catalytic activity were explored as well for the same Ru/RuS$_2$-BA-900@WC prepared with the mass ratio of 24/1. As shown in Fig. 5d, the Ru/RuS$_2$-BA-900@WC required overpotential of only 228 mV to reach 10 mA cm^{-2}, lower than 517 mV for Ru/RuS$_2$-BA-700@WC and 527 mV for Ru/RuS$_2$-BA-800@WC, respectively. Therefore, the carbonization temperature of 900 °C was undoubtedly the most appropriate one for optimizing the catalyst activity. The high temperature was more conducive to remove S atoms in carbocyclic rings, forming rich defect sites to improve the OER activity. The larger charge transfer resistance in Fig. 5e and the higher slope in Fig. 5f which demonstrated that the charge transfer of the Ru/RuS$_2$-BAs@WC prepared under 700 or 800 °C was seriously hindered and the reaction kinetics became slower. The electrochemical active areas of the Ru/RuS$_2$-BA-900@WC were evaluated by cyclic voltammetry curves at scanning rates of 25, 50, 75, 100, 125, and 150 mV s^{-1}, respectively. The double-layer capacitance in Fig. 5g and Fig. S11 in Supporting Information exhibits the active area of 26.9 mF cm^{-2}. Compared with catalytic activities in acidic media for noble-metal catalysts in recent reports, the Ru/RuS$_2$-BA-900@WC required a considerably lower overpotential to deliver the same 10 mA cm^{-2} (Fig. 5h) (Esquius et al. 2020; Feng et al. 2019; Guo et al. 2019; Sun et al. 2016; Wang et al. 2021a; Zhang et al. 2019).
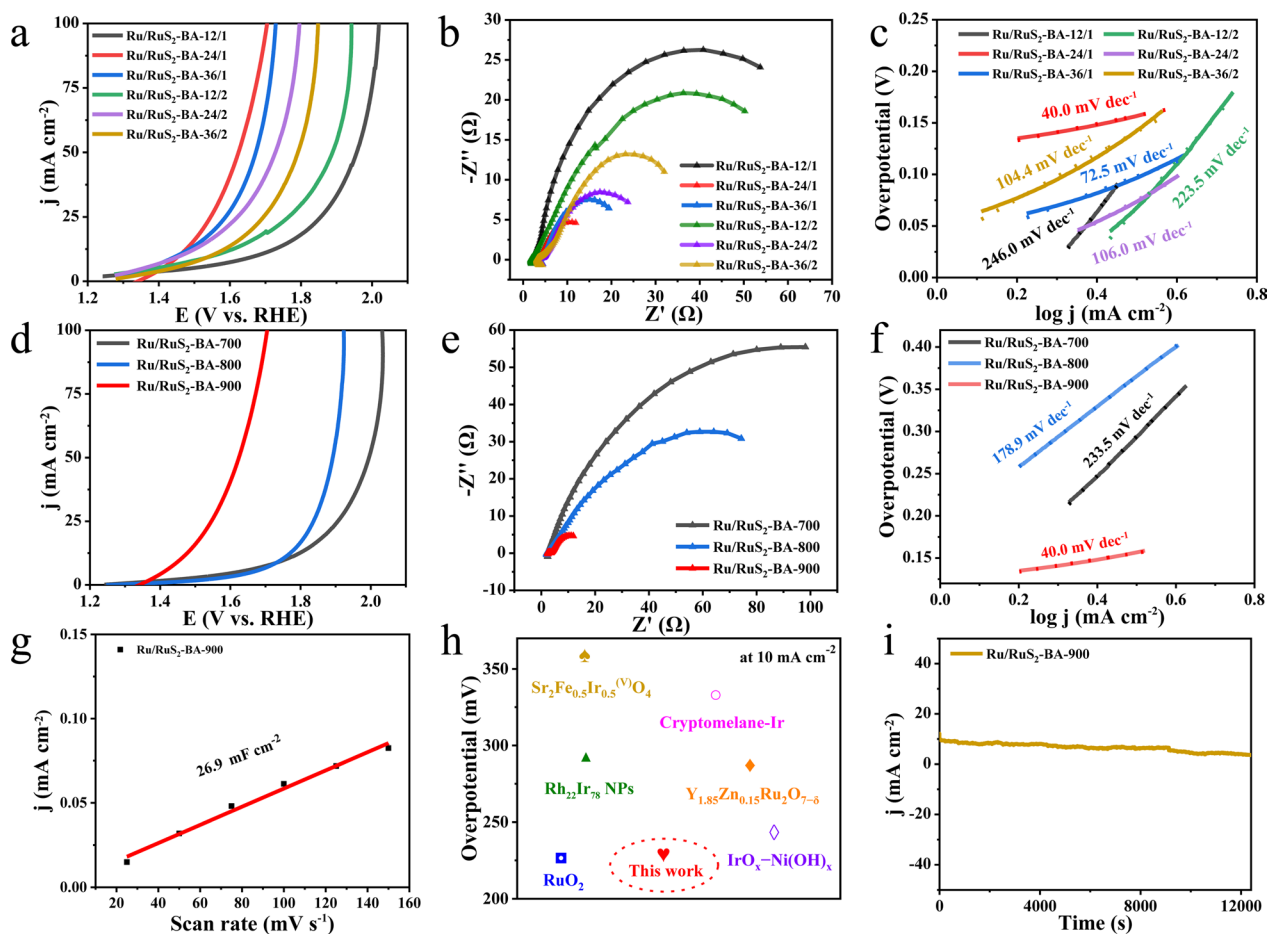
Fig. 5 **a** OER polarization curves, **b** EIS Nyquist plots, and **c** Tafel plots of Ru/RuS$_2$-BA with different mass ratios in 0.5 M H$_2$SO$_4$. **d** OER polarization curves, **e** EIS Nyquist plots, and **f** Tafel plots of Ru/RuS$_2$-BA with different carbonization temperature in 0.5 M H$_2$SO$_4$. **g** Evaluated C_{dl} values of Ru/RuS$_2$-BA. **h** Comparison diagram of overpotentials of Ru/RuS$_2$-BA with other works. **i** Chronoamperometry curves of Ru/RuS$_2$-BA-900

Comparisons of similar studies in recent years were carried out and are presented in Table S1 in Supporting Information. The OER activity of the Ru/RuS$_2$-BA@WC in acid electrolyte was significantly improved. The durability was also a vital parameter for the catalyst. The chronoamperometry test was conducted for the Ru/RuS$_2$-BA-900@WC at 10 mA cm^{-2}. Inspiringly, as shown in Fig. 5i, the Ru/RuS$_2$-BA-900@WC system exhibited an excellent durability for 12,390 s in 0.5 M H$_2$SO$_4$, with no perceptible decline of current density according to the observation of the chronoamperometry curve.

Based on the high activity and stability of the Ru/RuS$_2$-BA-900@WC in acidic electrolytes, it was innovatively proposed the structural design mechanism of Ru/RuS$_2$-BA-900, as shown in Fig. 6. As two types of natural precursors of derived carbon, the alginate and lignosulfonate were rich in hydroxyl, carboxyl, and sulfonate groups. In Fig. 6a, the lignin aerogel with 3D porous frameworks could be constructed after the freeze-drying for the lignosulfonate aqueous solution. Under coordination effect with the trivalent ruthenium, alginate could form the unique "egg-box" structure, which finally boosted the generation of lamellar aerogel units of 2D structures (Fig. 6b). Upon the synergic self-assembly, the composite polymer aerogel that consisted of alginate and lignosulfonate could exhibit the 2D/3D interpenetrating supramolecular configuration (Fig. 6c). Due to the in-situ carbonization effect at high temperatures, the composite polymer aerogel with 2D/3D structure was converted into the carbon aerogel with the similar structure, as seen in Fig. 6d. During the structural reconstruction, the microenvironment of the carbon layer and ruthenium center was adjusted optimally. As a result, the BA loaded with Ru/RuS$_2$ particles was synthetized ultimately. Notably, the coordination of ruthenium with two kinds of advanced precursors greatly increased the whole stability of the composite aerogel. Surprisingly, the in-situ carbonization also promoted the increase of the specific surface area of the carbon aerogel and the formation of numerous defective sites. The increased specific surface area
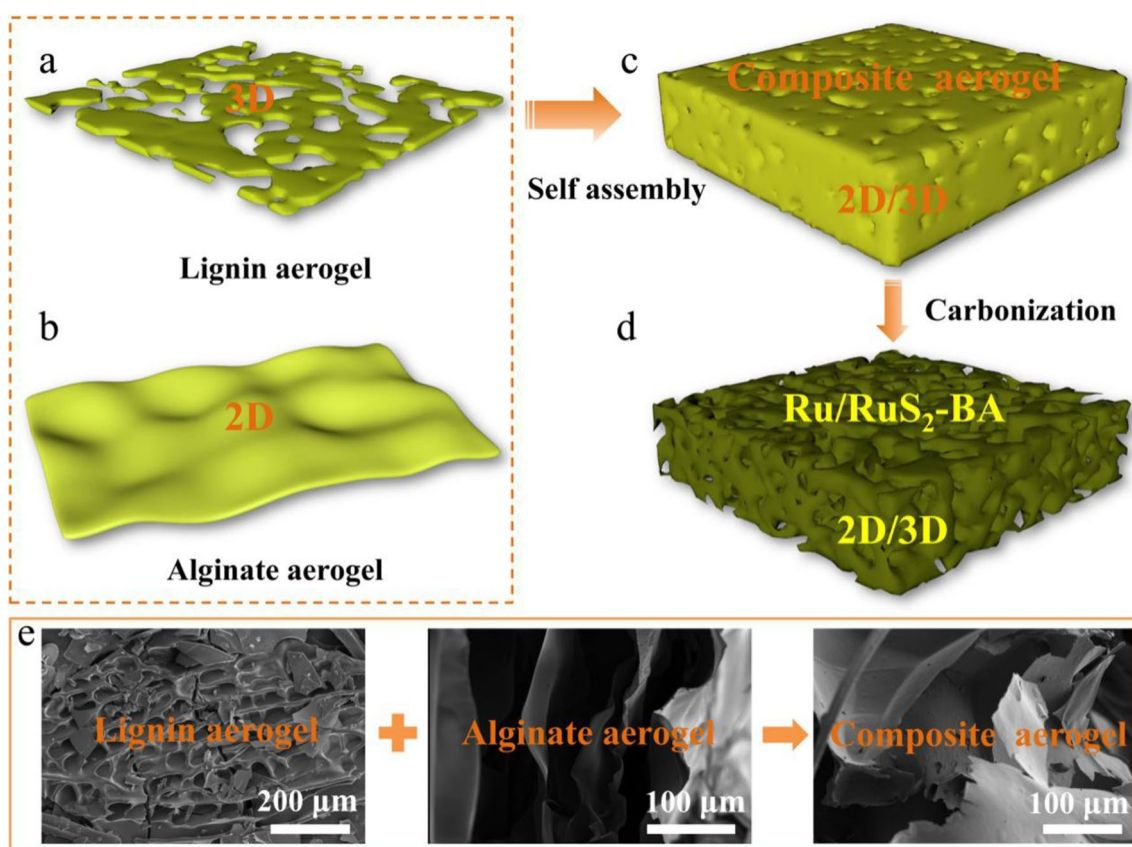
Fig. 6 Schematic illustration for structural design mechanism of Ru/RuS$_2$-BA. **a** Lignin aerogel with 3D structure, **b** alginate aerogel with 2D structure, **c** polymer aerogel with 2D/3D structure (alginate aerogel + lignin aerogel), and **d** carbon aerogel with 2D/3D structure that stemmed from the in-situ carbonization for the aforementioned polymer aerogel. **e** SEM images of lignin aerogel, alginate aerogel, and composite aerogel

in the carbon aerogel further boosted the transport capacity of electrolyte. The synergy of defective sites at carbon and Ru/RuS$_2$ heterostructure enhanced the activity and stability of the Ru/RuS$_2$-BA-900 integrator. The SEM images observed in Fig. 6e verified the proposed hypothesis for the 2D/3D structural design mechanism of the Ru/RuS$_2$-BA-900. The formed supramolecular configuration was integrated with the original alginate aerogel with 2D structure and lignin aerogel with 3D structure, thus remarkably improving efficiency of mass transfer during acidic OER.

4 Conclusions

In summary, the Ru/RuS$_2$ heterojunction confined at BA was synthesized using natural and sustainable biomass materials as precursors. Due to the induction effect of the "egg-box" structure in alginate and the self-template effect of lignosulfonate, the structural carbon aerogel loaded with Ru/RuS$_2$ particles was obtained triumphantly. The S atoms

that entered the carbon shells were partially removed during the high temperature treatment, leading to the generation of numerous defects at carbon. Due to the synergistic influence of the Ru/RuS$_2$ heterostructure and defective sites, the OER activity of the catalyst system was enhanced significantly. The Ru/RuS$_2$-BA-900@WC required overpotential of only 228 mV to deliver current density of 10 mA cm^{-2} in 0.5 M H$_2$SO$_4$. The inherent stable 2D/3D microstructure in Ru/RuS$_2$-BA-900@WC enhanced the cycling capacity and showed a high stability for over 12,000 s in 0.5 M H$_2$SO$_4$. This work opens a novel strategy to design and synthetize high-efficiency acidic OER electrocatalysts by jointly using marine and terrestrial plants as carbon sources. The proposed approach could further advance the structural design of various biochar-based electrocatalysis for hydrogen evolution, oxygen reduction, and nitrogen reduction reactions.

Declarations

References

Chen X, Bai Y, Shen X, Peng H, Zhang Q (2020) Sodiophilicity/potassiophilicity chemistry in sodium/potassium metal anodes. J Energy Chem 51:1–6

Chen H, Zou Y, Li J, Zhang K, Xia Y, Hui B, Yang D (2021) Wood aerogel-derived sandwich-like layered nanoelectrodes for alkaline overall seawater electrosplitting. Appl Catal B Environ 293:120215

Chen X, Zhang L, Xu W, Ding X, Chen S, She X, Guo X, Dong C-L, Huang Y, Zhang L, Shen S, Yang D (2022) Biochar aerogel decorated with thiophene S manipulated 5-membered rings boosts nitrogen fixation. Appl Catal B Environ 313:121425

Ding C, Liu Y, Xie P, Lan J, Yu Y, Fu X, Yang X, Zhong W (2021) A novel carbon aerogel enabling respiratory monitoring for bio-facial masks. J Mater Chem A 9:13143–13150

Esquius JR, Algara-Siller G, Spanos I, Freakley SJ, Schlogl R, Hutchings GJ (2020) Preparation of solid solution and layered IrOx-Ni(OH)$_2$ oxygen evolution catalysts: toward optimizing iridium efficiency for OER. ACS Catal 10:14640–14648

Fan Z, Jiang J, Ai L, Shao Z, Liu S (2019) Rational design of ruthenium and cobalt-based composites with rich metal-insulator interfaces for efficient and stable overall water splitting in acidic electrolyte. ACS Appl Mater Inter 11:47894–478903

Feng Q, Wang Q, Zhang Z, Xiong Y, Li H, Yao Y, Yuan X, Williams MC, Gu M, Chen H, Li H, Wang H (2019) Highly active and stable ruthenate pyrochlore for enhanced oxygen evolution reaction in acidic medium electrolysis. Appl Catal B Environ 244:494–501

Gabhi R, Basile L, Kirk DW, Giorcelli M, Tagliaferro A, Jia CQ (2020) Electrical conductivity of wood biochar monoliths and its dependence on pyrolysis temperature. Biochar 2:369–378

Gao S, Zhu Y, Wang J, Zhang F, Li J, Jin J (2018) Layer-by-Layer construction of Cu^{2+}/alginate multilayer modified ultrafiltration membrane with bioinspired superwetting property for high-efficient crude-oil-in-water emulsion separation. Adv Funct Mater 28:1801944

Goryaeva AM, Lapointe C, Dai CD, Deres J, Maillet JB, Marinica MC (2020) Reinforcing materials modelling by encoding the structures of defects in crystalline solids into distortion scores. Nat Commun 11:32943615

Guo H, Fang Z, Li H, Fernandez D, Henkelman G, Humphrey SM, Yu G (2019) Rational design of rhodium-iridium alloy nanoparticles as highly active catalysts for acidic oxygen evolution. ACS Nano 13:13225–13234

Hua L, Cheng T, Liang Z, Wei T (2022) Investigation of the mechanism of phytate-modified biochar-catalyzed persulfate degradation of ponceau 2R. Biochar 4:1–13

Hui B, Zhang K, Xia Y, Zhou C (2020) Natural multi-channeled wood frameworks for electrocatalytic hydrogen evolution. Electrochim Acta 330:135274

Hui B, Li J, Lu Y, Zhang K, Chen H, Yang D, Cai L, Huang Z (2021) Boosting electrocatalytic hydrogen generation by a renewable porous wood membrane decorated with Fe-doped NiP alloys. J Energy Chem 56:23–33

Humagain G, MacDougal K, MacInnis J, Lowe JM, Coridan RH, MacQuarrie S, Dasog M (2018) Highly efficient, biochar-derived molybdenum carbide hydrogen evolution electrocatalyst. Adv Energy Mater 8:1801461

Jiang Z, Zou Y, Li Y, Kong F, Yang D (2021) Environmental life cycle assessment of supercapacitor electrode production using algae derived biochar aerogel. Biochar 3:701–714

Kargarzadeh H, Huang J, Lin N, Ahmad I, Mariano M, Dufresne A, Thomas S, Galeski A (2018) Recent developments in nanocellulose-based biodegradable polymers, thermoplastic polymers, and porous nanocomposites. Prog Polym Sci 87:197–227

Lei T, Chen W, Lv W, Huang J, Zhu J, Chu J, Yan C, Wu C, Yan Y, He W, Xiong J, Li Y, Yan C, Goodenough JB, Duan X (2018) Inhibiting polysulfide shuttling with a graphene composite separator for highly robust lithium-sulfur batteries. Joule 2:2091–2104

Li M, Wang H, Zhu W, Li W, Wang C, Lu X (2020a) RuNi nanoparticles embedded in N-doped carbon nanofibers as a robust bifunctional catalyst for efficient overall water splitting. Adv Sci 7:1901833

Li Y, Wang Y, Lu J, Yang B, San X, Wu Z (2020b) 2D intrinsically defective RuO$_2$/graphene heterostructures as all-pH efficient oxygen evolving electrocatalysts with unprecedented activity. Nano Energy 78:105185

Li R, Wang H, Hu F, Chan K, Liu X, Lu Z, Wang J, Li Z, Zeng L, Li Y, Wu X, Xiong Y (2021a) IrW nanochannel support enabling ultrastable electrocatalytic oxygen evolution at 2 A cm^{-2} in acidic media. Nat Commun 12:3540

Li Y, Wang J, Fan S, Wang F, Shen Z, Duan H, Xu J, Huang Y (2021b) Nitrogen-doped hierarchically porous carbon spheres for low concentration CO_2 capture. J Energy Chem 53:168–174

Liang L, Xi F, Tan W, Meng X, Hu B, Wang X (2021) Review of organic and inorganic pollutants removal by biochar and biochar-based composites. Biochar 3:255–281

Lin Y, Tian Z, Zhang L, Ma J, Jiang Z, Deibert BJ, Ge R, Chen L (2019) Chromium-ruthenium oxide solid solution electrocatalyst for highly efficient oxygen evolution reaction in acidic media. Nat Commun 10:162

Liu J, Zheng Y, Jiao Y, Wang Z, Lu Z, Vasileff A, Qiao SZ (2018) NiO as a bifunctional promoter for RuO_2 toward superior overall water splitting. Small 14:1704073

Liu Y, Li X, Zhang Q, Li W, Xie Y, Liu H, Shang L, Liu Z, Chen Z, Gu L, Tang Z, Zhang T, Lu S (2020) A general route to prepare low-ruthenium-content bimetallic electrocatalysts for pH-universal hydrogen evolution reaction by using carbon quantum dots. Angew Chem Int Ed 59:1718–1726

Liu X, Cui X, Dastafkan K, Wang H, Tang C, Zhao C, Chen A, He C, Han M, Zhang Q (2021a) Recent advances in spinel-type electrocatalysts for bifunctional oxygen reduction and oxygen evolution reactions. J Energy Chem 53:290–302

Liu Y, Ding C, Yan X, Xie P, Xu B, Chen L, Lin Y, Liu C, Yu Y, Lin Y (2021b) Interface-strain-confined synthesis of amorphous TiO_2 mesoporous nanosheets with stable pseudocapacitive lithium storage. Chem Eng J 420:129894

Liu Z, Hao N, Wang Y, Dou C, Lin F, Shen R, Bura R, Hodge D, Dale B, Ragauskas A, Yang B, Yuan J (2021c) Transforming biorefinery designs with "plug-in processes of lignin" to enable economic waste valorization. Nat Commun 12:3912

Lu L, Yu W, Wang Y, Zhang K, Zhu X, Zhang Y, Wu Y, Ullah H, Xiao X, Chen B (2020) Application of biochar based materials in environmental remediation: from multi-level structures to specific devices. Biochar 2:1–31

Luo N, Chen C, Yang D, Hu W, Dong F (2021) S defect-rich ultrathin 2D MoS_2: the role of S point-defects and S stripping-defects in the removal of Cr (VI) via synergistic adsorption and photocatalysis. Appl Catal B Environ 299:120664

Meng X, Tian X, Xia Y, Xiong Z (2021) Multifunctional alginate-based carbon aerogels for oil–water mixture and emulsion separation. J Disper Sci Technol 1–8

Musiienko A, Ceratti DR, Pipek J, Brynza M, Elhadidy H, Belas E, Betusiak M, Delport G, Praus P (2021) Defects in hybrid perovskites: the secret of efficient charge transport. Adv Funct Mater 31:2104467

Pascuzzi MEC, Goryachev A, Hofmann JP, Hensen EJM (2020) Mn promotion of rutile TiO_2-RuO_2 anodes for water oxidation in acidic media. Appl Catal B Environ 261:118225

Sakhiya A, Anand A, Kaushal P (2020) Production, activation, and applications of biochar in recent times. Biochar 2:253–285

Shen W, Zhao G, Zhang X, Bu F, Yun J, Tang J (2020) Using dual microresonant cavity and plasmonic effects to enhance the photovoltaic efficiency of flexible polymer solar cells. Nanomaterials 10:944

Su J, Ge R, Jiang K, Dong Y, Hao F, Tian Z, Chen G, Chen L (2018) Assembling ultrasmall copper-doped ruthenium oxide nanocrystals into hollow porous polyhedra: highly robust electrocatalysts for oxygen evolution in acidic media. Adv Mater 30:1801351

Sun W, Cao L, Yang J (2016) Conversion of inert cryptomelane-type manganese oxide into a highly efficient oxygen evolution catalyst via limited Ir doping. J Mater Chem A 4:12561–12570

Tian X, Zhu H, Meng X, Wang J, Zheng C, Xia Y, Xiong Z (2020) Amphiphilic calcium alginate carbon aerogels: Broadspectrum adsorbents for ionic and solvent dyes with multiple functions for decolorized oil–water separation. ACS Sustain Chem Eng 8:12755–12767

Wang M, Wang F (2019) Catalytic scissoring of lignin into aryl monomers. Adv Mater 31:1901866

Wang M, Zhang X, Li H, Lu J, Liu M, Wang F (2018) Carbon modification of nickel catalyst for depolymerization of oxidized lignin to aromatics. ACS Catal 8:1614–1620

Wang T, Hu S, Wu D, Zhao W, Yu W, Wang M, Xu J, Zhang J (2021a) Boosting the capacity of biomass-based supercapacitors using carbon materials of wood derivatives and redox molecules from plants. J Mater Chem A 9:11839–11852

Wang Z, Xiao B, Lin Z, Shen S, Xu A, Du Z, Chen Y, Zhong W (2021b) In-situ surface decoration of RuO_2 nanoparticles by laser ablation for improved oxygen evolution reaction activity in both acid and alkali solutions. J Energy Chem 54:510–518

Xia Y, Wu W, Wang H, Rao S, Zhang F, Zou G (2020) Amorphous RuS_2 electrocatalyst with optimized active sites for hydrogen evolution. Nanotechnology 31:145401

Xu Y, Du C, Shen Q, Huang J, Zhang X, Chen J (2021) Well-dispersed pyrite-type RuS_2 nanocrystals anchored on porous nitrogen and sulfur co-doped hollow carbon spheres for enhanced alkaline hydrogen evolution. Chem Eng J 417:129318

Yan M, Jiang Q, Zhang T, Wang J, Yang L, Lu Z, He H, Fu Y, Wang X, Huang H (2018) Three-dimensional low-defect carbon nanotube/nitrogen-doped graphene hybrid aerogel-supported Pt nanoparticles as efficient electrocatalysts toward the methanol oxidation reaction. J Mater Chem A 6:18165–18172

Yang Q, Zhang C, Dong B, Cui Y, Wang F, Cai J, Jin P, Feng L (2021) Synergistic modulation of nanostructure and active sites: Ternary Ru & Fe-WO$_x$ electrocatalyst for boosting concurrent generations of hydrogen and formate over 500 mA cm^{-2}. Appl Catal B Environ 296:120359

Ye J, Liu L, Oakdale J, Lefebvre J, Bhowmick S, Voisin T, Roehling JD, Smith WL, Ceron MR, Ham JV, Aji LBB, Biener MM, Wang YM, Onck PR, Biener J (2021) Ultra-low-density digitally architected carbon with a strutted tube-in-tube structure. Nat Mater 20:1498

Zhang R, Dubouis N, Osman MB, Yin W, Sougrati MT, Corte DAD, Giaume D, Grimaud A (2019) Dissolution/precipitation equilibrium on the surface of iridium-based perovskites controls their activity as oxygen evolution reaction catalysts in acidic media. Angew Chem Int Ed 58:4571–4575

Zhang L, Jang H, Liu H, Kim M, Yang D, Liu S, Liu X, Cho J (2021) Sodium-decorated amorphous/crystalline RuO_2 with rich oxygen vacancies: a robust pH-universal oxygen evolution electrocatalyst. Angew Chem Int Ed 60:18821–18829

Zhao X, Yu X, Xin S, Chen S, Bao C, Xu W, Xue J, Hin B, Zhang J, She X, Yang D (2022) Enhanced oxygen reduction reaction for Zn-air battery at defective carbon fibers derived from seaweed polysaccharide. Appl Catal B Environ 301:120785

Zhu J, Guo Y, Liu F, Xu H, Gong L, Shi W, Chen D, Wang P, Yang Y, Zhang C, Wu J, Luo J, Mu S (2021) Regulative electronic states around ruthenium/ruthenium disulphide heterointerfaces for efficient water splitting in acidic media. Angew Chem Int Ed 60:12328–12334

Zou Y, Yu G, Hin B, Yang X, Liu H, Chen S, Cai R, Sun J, Zhang X, Yang D (2020) Nitrogen and sulfur vacancies in carbon shell to tune charge distribution of $Co_6Ni_3S_8$ core and boost sodium storage. Adv Energy Mater 10:1904147

Authors and Affiliations

Bin Hui[1] · Hongjiao Chen[1] · Chengfeng Zhou[1] · Liping Cai[2] · Kewei Zhang[1] · Fengyu Quan[1] · Dongjiang Yang[1]

✉ Bin Hui
  huibin@qdu.edu.cn

✉ Dongjiang Yang
  d.yang@qdu.edu.cn

[1] State Key Laboratory of Bio-Fibers and Eco-Textiles, Shandong Collaborative Innovation Center of Marine Biobased Fiber and Ecological Textile, Institute of Marine Biobased Materials, School of Materials Science and Engineering and School of Environmental Science and Engineering, Qingdao University, Qingdao 266071, People's Republic of China

[2] Department of Mechanical Engineering, University of North Texas, Denton, TX 76207, USA